ISSUE: February 2020

GaN-Based Wireless Power Enables Efficient, Seamless Multi-Device Charging

by Daniel Costinett, Jie Li, Jingjing Sun and Peter Pham, The University of Tennessee, Knoxville, Tenn.

For consumer mobile electronics, wireless power transfer (WPT) promises to revolutionize the way users interact with their devices. Ubiquitous, seamless charging is expected to reduce onboard battery storage requirements and untether mobile devices from periodic wired charging requirements.

At present, commercial implementations of wireless power transfer are largely limited to low power, low efficiency, and a charging paradigm where each device must be well aligned with a dedicated charger. Though the technology continues to progress, this approach fails to capitalize on the promise of spatial freedom and effortless, pervasive charging which make wireless power transfer attractive.

Fig. 1 shows the target application and experimental demonstration loads used in this work. The goal is to design a workstation in which a single transmitter seamlessly charges electronic devices of varying power levels, simultaneously, when placed in arbitrary coplanar positions above a 0.5-m x 0.5-m charging area.

This work, in collaboration with Power America, leverages the capabilities of wide-bandgap semiconductors, particularly gallium nitride (GaN) transistors, to enable new design paradigms for WPT systems. In particular, the focus here is on achieving comparable power levels and efficiency to traditional wired charging, while allowing unobtrusive charging of many devices simultaneously.

This article begins by explaining the principles of operation behind popular WPT systems that use inductive power transfer. A simple model is presented and used to explain the constraints on power transfer efficiency, and the techniques that can be used to optimize efficiency in the case where a single load is being powered and where there are multiple loads. This leads to the proposal of an alternative approach, which achieves uniform coupling to multiple devices over a larger charging area for spatial freedom, while obtaining very high quality factor coils to allow high efficiency power transfer.

The article then delves into the details of designing such a single-transmitter, multi-receiver system for wireless charging. First, it describes the constraints on coil design and how these influence efficiency. The choice of operating frequency figures prominently here, and sets the stage for selection of a higher operating frequency (6.78 MHz).

Then a conventional end-to-end WPT system is presented to explain the impact of the various power stages on overall system efficiency. Because the conventional system only achieves about 65% overall efficiency, an alternative system structure is proposed that eliminates some of the cascaded stages, boosting efficiency to 85% or higher. This system structure is made feasible by the use of GaN transistors which excel at high frequency switching with large voltage bias. Requirements for implementing this alternative WPT system design are then described, followed by detailed discussion of the prototype design and presentation of experimental results.

The prototype system is designed to supply 100 W to five loads, while targeting 90% full load efficiency from ac line to dc output and a transmitter power density greater than 25 W/in^3. Two different receiver designs are presented. A high-power receiver meant to be integrated into the application is offered for loads >1 W, while a <1-W receiver is given as a retrofit solution for low-power applications. Finally, some ongoing research is discussed relating to transmission of wireless power to metal-body receivers as would be required in laptops.

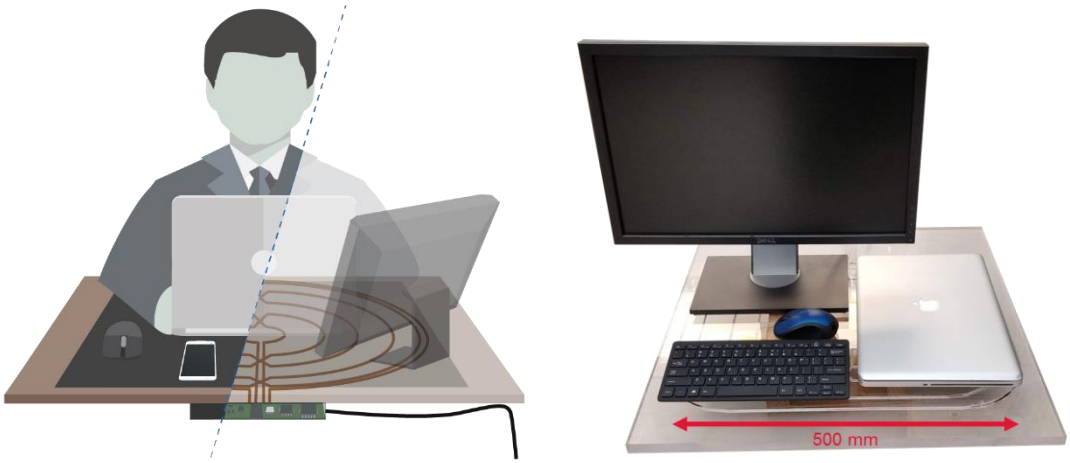

(a) (b)

Fig. 1. The multi-device charging scenario which is the focus of this work (a) and an experimental platform with test loads (b).

Fundamentals Of WPT

Inductive Power Transfer

Though multiple approaches to WPT are being pursued in research, inductive power transfer (IPT) has emerged as the most popular approach to WPT over relatively short distances, such as through a table. IPT uses a pair of magnetically coupled coils to wirelessly transfer power through a nonconductive medium.

The approach is modeled through the simplified circuit of Fig. 2 wherein a transmitter v_{tx} provides an ac current i_p in the primary coil L_p. This current induces a voltage on the secondary coil L_s of a single receiver which is transferred to the ac load, R_L. The resistances R_p and R_s model any parasitic resistance in the primary and secondary loop, predominately the resistance of the two coils. Impedances Z_p and Z_s model any additional reactive components inserted into each loop.

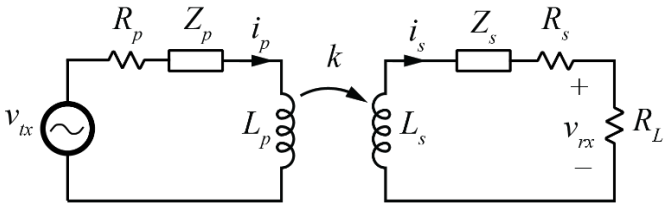

Fig. 2. Simplified fundamental model of a magnetically coupled WPT circuit.

For a single-frequency, sinusoidal ac source v_{tx} operating at frequency ω, the efficiency of the circuit in Fig. 2 is maximized[1] when $Z_s = j\omega L_s$ and

$$R_L = R_s\sqrt{1+k^2\frac{\omega L_p}{R_p}\frac{\omega L_s}{R_s}} = R_s\sqrt{1+k^2Q_pQ_s} \quad (1)$$

At this load resistance, the maximum efficiency is

$$\eta_{\max} = \frac{k^2 Q_p Q_s}{\left(1 + \sqrt{1 + k^2 Q_p Q_s}\right)^2} \quad (2)$$

Examining this expression, achieving high efficiency requires that the WPT coils be designed in such a way as to maximize the term $k^2Q_pQ_s$ i.e. both coils must exhibit high quality factor and should be tightly coupled. As an example, achieving 98% efficiency through the coils requires $k^2Q_pQ_s \geq 10{,}000$.

Given this simplified analysis of the system, two pathways to high efficiency are possible: increasing the coupling factor k through the geometric design of the system, and increasing coil quality factor through both the coil geometry and electrical design of the system. Unfortunately, the former often runs counter to the goal of seamless multi-device charging. Fig. 3 gives approximate ranges for k for both a one-to-one, tightly coupled WPT link and a loosely coupled system where one transmitter charges multiple receivers.

(a) *(b)*

Fig. 3. Example coupling coefficients for one-to-one charging (a) and multi-receiver WPT (b).

Various techniques can be used to increase coupling within either paradigm, including the use of high-permeability magnetic material or other field-shaping techniques. However, in the multi-receiver case, where each receiver is physically separate and coplanar, a lower coupling coefficient between the transmitter and any one receiver will be incurred. Parasitic cross-coupling between receivers exists in Fig. 3b, but is mitigated in-application by requirements for shielding the internal electronics of the receiver and the practical mechanical limits on the proximity of individual receivers.

An alternative approach, shown in Fig. 4, seeks to recapture the high coupling coefficient of the one-to-one case while allowing multiple receivers and a larger charging area by segmenting the transmitter into smaller, individually driven coils. Though superior coupling is achievable, this approach may complicate sensing, control, and thermal designs due to parasitic coupling between adjacent transmitter coils. As such, this work retains the paradigm of Fig. 3b, instead designing towards higher frequencies where an increase in coil quality factors Q_p and Q_s can offset the reduced coupling coefficient to maintain high efficiency.

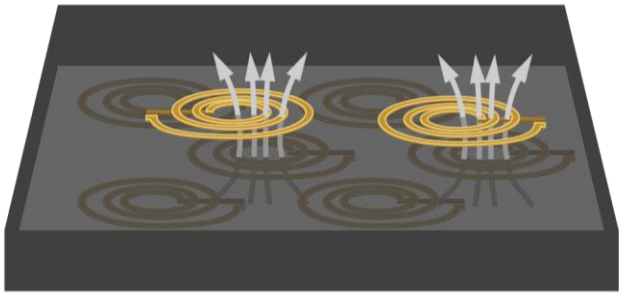

Fig. 4. Example multi-transmitter, multi-receiver WPT system.

WPT Coil Design

To achieve the target system of Fig. 1 with high efficiency, every effort must be made to increase the quality factor of transmitter and receiver coils. To examine the design implications, simple models of inductance[2] and resistance[3] are used to approximate a multi-turn circular spiral transmitter coil with a 500-mm diameter using 16 AWG copper wire. The results are shown in Fig. 5a for varying numbers of turns and WPT frequency.

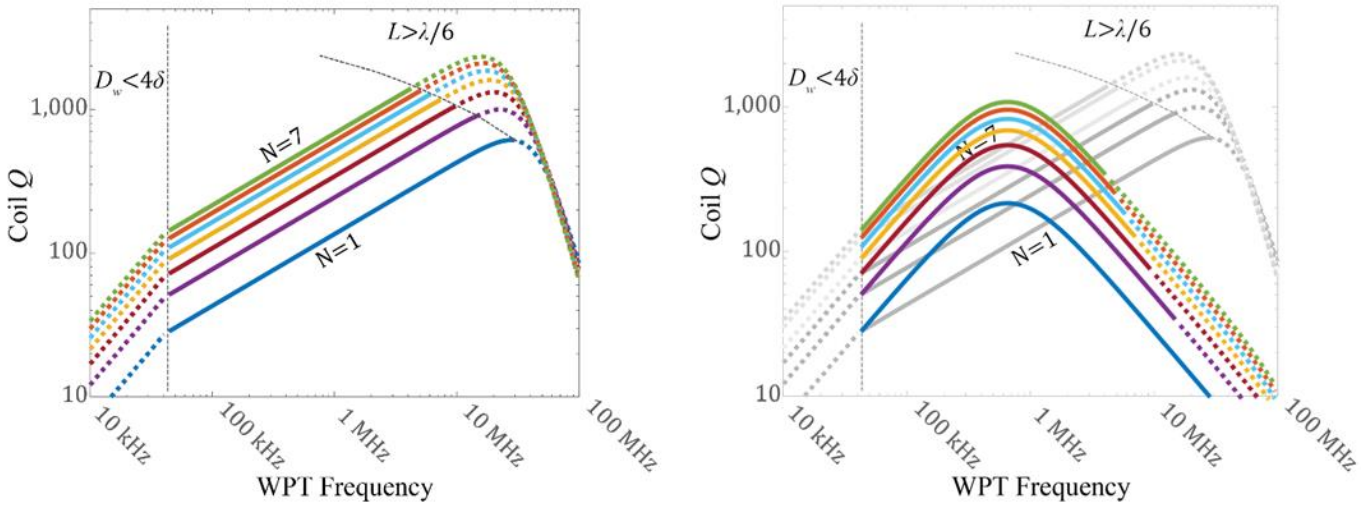

Fig. 5. Approximate coil quality factors with solid-core wire (a) and 48-AWG strand Litz wire (b).

The quality factor $Q = \omega L/R_{ac}$ increases with frequency over a limited range. The reactance in the numerator increases in proportion to frequency; the resistance in the denominator is constant at low frequency where skin effect is negligible, then increases proportionally to $\sqrt{\omega}$ at intermediate frequencies where skin effect dominates.

As the frequency continues to increase, the design eventually reaches the point where the overall coil length approaches $\lambda/4$ and the resistance increases in proportion to ω^4 due to radiation effects. The designs in Fig. 5b are conservatively limited to $\lambda/6$ to prevent excessive radiation and associated safety concerns. For $N > 1$ turns, this limits the radiated power to less than 5% of the total coil loss.

Though Litz wire can assist in reducing the skin-depth-related losses at low frequency, it becomes prohibitively expensive at high frequencies. Using the model detailed in reference [4] Fig. 5b shows the approximate resistance of the same coils for 48-AWG strand Litz wire and the same total wire area. At higher strand gauge, Litz wire becomes competitive over a wider frequency range, but may become prohibitively expensive.

Using the same parameters, the efficiency, optimal load resistance, transmitter voltage amplitude, and primary-side current amplitude are shown in Fig. 6 for varying k and frequency. Voltage and current amplitude are evaluated for a design with $N = 3$ operating at a power level of 100 W. For each coupling factor, maximum efficiency occurs in the high-frequency range where solid-core wire outperforms equivalent-AWG Litz.

This highly simplified analysis favors system operation in the multi-megahertz frequency range when pursuing high efficiency through high quality factor coils. Again referring to Fig. 6, note that in this frequency range the optimal load resistance is large, resulting in high-voltage and low-current operation at the transmitter for the same power level. Operation in this range is enabled by high-voltage, fast-switching GaN devices, as discussed further in the following section.

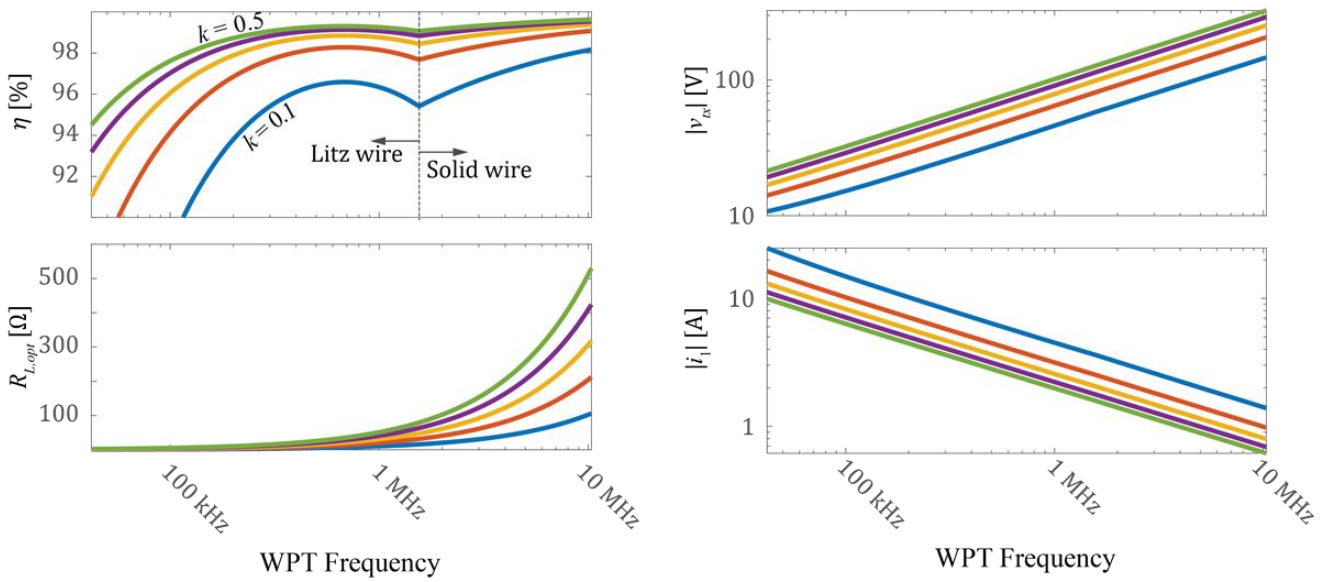

Fig. 6. Comparison of various parameters for a 100-W, N = 3 transmitter coil.

While pursuit of high-efficiency power transfer heavily influences the choice of operating frequency, human safety and electromagnetic compliance also constrain the WPT frequency selection. A summary of some relevant standards is given in Fig. 7. Compliance standards do not regulate within the ISM band at 6.78 MHz ± 15 kHz. However, ICNIRP 2010 still imposes constraints on field generation in this range with a maximum magnetic flux density of 27 μT, though additional considerations may be needed.[5]

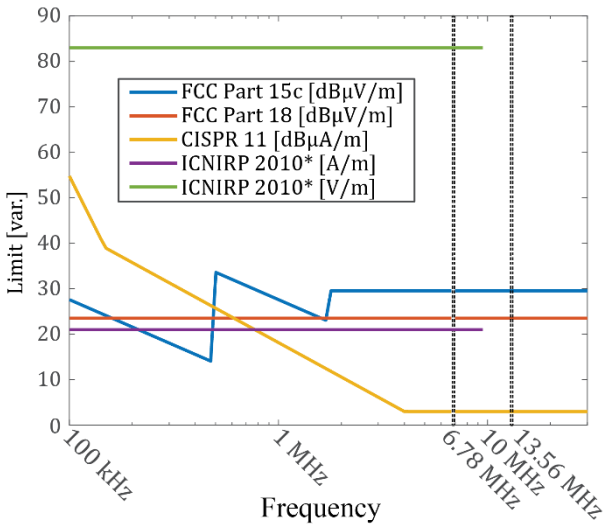

Fig. 7. EMI and human safety field limits.

The combination of electrical performance and compliance standards motivates the use of 6.78 MHz as a candidate frequency for this application.

WPT Standards

Much of the discussion in the previous section mirrors the current contrast between the two commercial WPT standards. The Qi standard[6] developed by the Wireless Power Consortium focuses on low-frequency 87- to 205-kHz operation. The Airfuel Resonant standard[7] developed by the Airfuel Alliance instead focuses on operation at 6.78 MHz, advocating benefits in the ability to accommodate greater spatial freedom. Beyond operating frequency, each standard includes many additional regulations targeting compliance, interoperability, regulation and communication.

Power Stage Design

Though the coil-to-coil efficiency, as modeled by the circuit of Fig. 2, is often one of the limiting factors, the overall efficiency can be much lower due to the additional conversion stages required to implement a complete WPT system.

An example implementation of the complete charger, from ac line to battery, is shown in Fig. 8. Assuming an output power greater than 75 W, a PFC rectifier is used, with an additional dc-dc converter used to generate a low-voltage output. In the transmitter, a soft-switching class E inverter is used, with switching frequency equal to the WPT frequency. An additional dc-dc converter provides regulation capability and design freedom in the use of low-voltage fast-switching silicon transistors in the class E inverter.

After the coils and impedance matching networks, the receiver is comprised of a diode rectifier followed by a dc-dc converter. This dc-dc converter's conversion ratio allows the battery charger load to be transformed, over a limited range, to match the optimal load resistance of the WPT coils as given in equation (1).

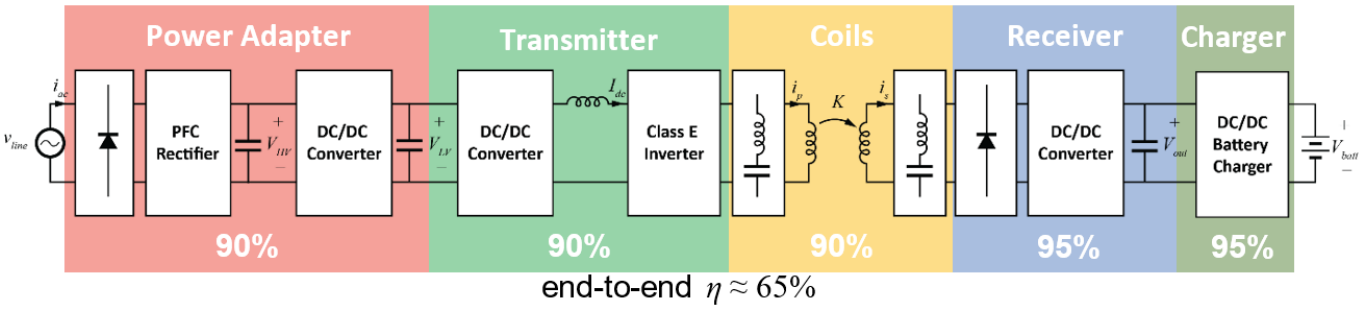

Fig. 8. Example end-to-end WPT system.

Fig. 8 additionally shows approximate efficiencies of each stage. Though each individual stage exhibits over 90% efficiency, the overall end-to-end efficiency is slightly above 65%. A survey of commercial products completed at the beginning of this project confirms the paradigm, as shown in Fig. 9. At the time, no end-to-end 100-W WPT system was widely available, so systems of varying power level are included. Due to the number of cascaded conversion stages, significant room for improvement is available through end-to-end system design.

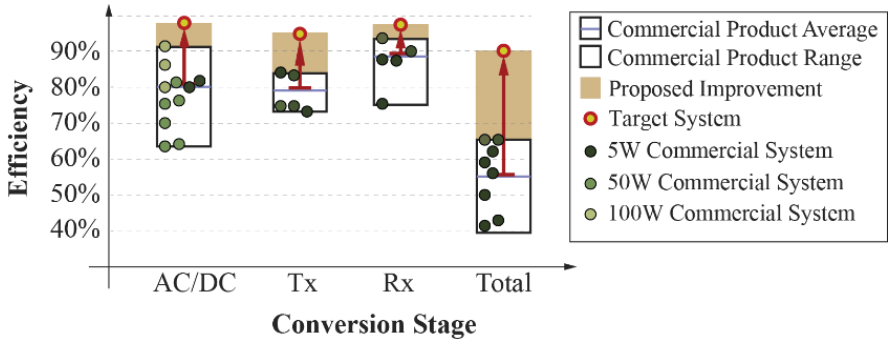

Fig. 9. A commercial product survey of WPT stages.

One feasible alternative structure is shown in Fig. 10, wherein all dc-dc converters have been eliminated save for the battery charger. Additionally, projected design improvements in the coils and power stages lead to a possible end-to-end efficiency of 85%, or nearly 90% from ac line to the battery charger input. There is further potential for consolidation, e.g. through a single-stage ac-to-RF converter on the primary[8] or an active rectifier with both output regulation and impedance matching capabilities (e.g. reference [9]).

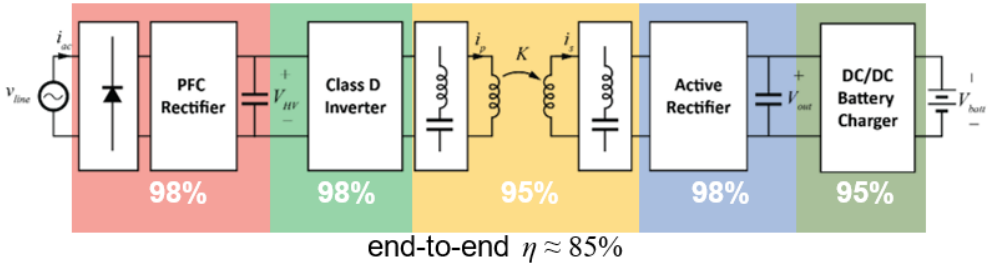

Fig. 10. WPT system with fewer conversion stages.

To make this design feasible, the transmitter and receiver design must change substantially. Without complication of the PFC rectifier design, the elimination of a dc-dc stage before the inverter indicates that the inverter will need to operate at a megahertz switching frequency, with a 200-V+ bus voltage. While this is well-matched to the optimal loading in the multi-megahertz range as shown in Fig. 6, the feasibility of this solution is predicated on the use of high-voltage, fast-switching transistors in the inverter stage.

Similarly, eliminating the dc-dc converter after the rectifier indicates that the previous diode rectifier may need to be replaced with a controllable active rectifier to retain the ability to present optimal loading as in equation (1).

To examine the implications of this design on power transistor selection, a baseline design of the class D inverter using a half-bridge inverter operating at 50% duty cycle at full load is considered in Fig. 11. At a 200-V+ bus voltage and a 6.78-MHz switching frequency, soft switching is required to prevent excessive switching loss, and possible failure. In this idealized examination, zero voltage switching of both transistors is assumed to occur at all operating points without any penalty in the conduction loss of the devices. Remaining loss mechanisms are modeled as only conduction loss and gate driver loss, per the following equations.

$$P_{cond} = {i_{p,rms}}^2 r_{on} \geq \left(\frac{P_{out}}{\sqrt{2}} \cdot \frac{2}{V_{HV}} \cdot \frac{\pi}{2}\right)^2 \quad (3)$$

$$P_g = 2 Q_g V_{gs} f_s \quad (4)$$

For a P_{out} = 100-W design with V_{HV} = 200 V and f_s = 6.78 MHz, these two losses are calculated for a variety of commercial discrete transistors in Fig. 11. For devices with a rated V_{ds} below 300 V, a minimum number of series devices are assumed in a multilevel topology. For a maximum allowable loss of 2 W, as required to meet the 98% efficiency target in Fig. 10, only GaN FET devices are capable of meeting the performance requirements in a two-level topology. In contrast, only with considerable additional effort, through use of a multilevel topology or resonant/undervoltaged gate-driving design, can silicon MOSFETs meet the required efficiency in this application.

Regardless of design effort, GaN FET devices have the potential to significantly outperform silicon in this application. Within reasonable bounds on complexity, the specifications detailed in Fig. 10 may be possible only with the use of GaN FET devices.

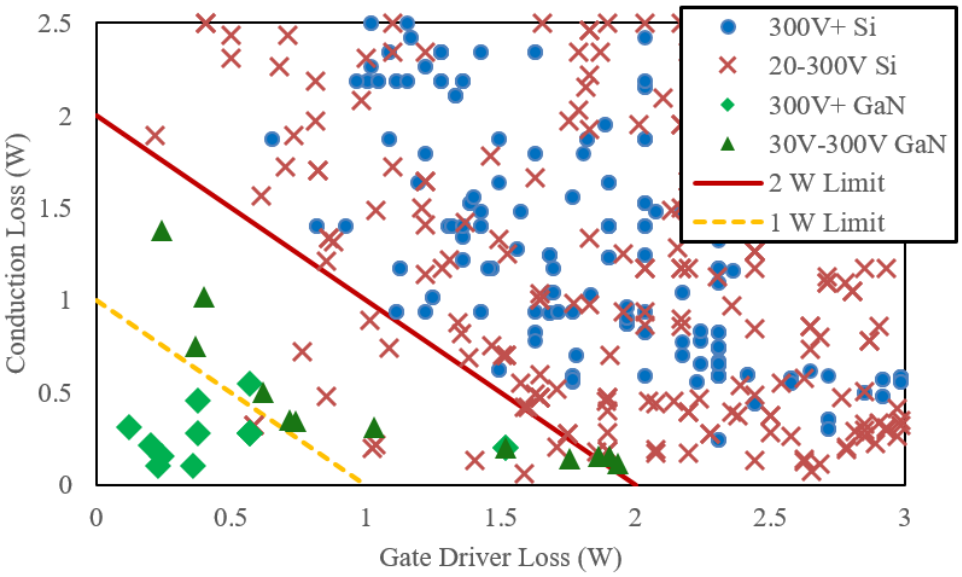

Fig. 11. Simplified loss analysis of silicon and GaN devices in a 6.78-MHz, 100-W half-bridge configuration.

Multi-Receiver GaN-Based WPT System Prototype Design

The prototype system in Fig. 1 is designed to supply 100 W to five loads with an approximate power budget shown in Table 1. The system is designed with a 6.78-MHz WPT frequency, and targets 90% full load efficiency from v_{line} to V_{out} and a transmitter power density greater than 25 W/in^3. Two different receiver designs are included: a high-power design for loads >1 W which would require integration into the body of the devices and a low-power <1-W retrofit solution, which can adapt battery-powered receivers to WPT operation without modification.

Table 1. Power budget for example loads.

Design Class	Load	Power
High power	Laptop	50 W
	Monitor	50 W
Low power	Keyboard	< 1 W
	Mouse	< 1W

Multi-Receiver Decoupling

To achieve the desired charging flexibility, the system must be designed to supply power with limited impact from the spatial positioning of the receivers and exhibit limited cross-channel disturbance. For the latter, dynamic changes in the impedance presented to the transmitter by one load should not affect adjacent loads. Conceptually, these application requirements can be met when

1. The transmitter design achieves a constant coil-current amplitude independent of load impedance.
2. The coil design results in a constant flux coupled to the receiver independent of spatial positioning.

Combined, these two characteristics will yield seamless multi-device charging if negligible cross-coupling exists between the receivers. Though cross-coupling can be significant between coplanar coils, it is limited in applications where receivers are adequately shielded and placed sufficiently far apart, as is likely mandated by the physical constraints of the devices they are embedded within.

For example, a receiver embedded within a phone may be inset from the phone edges by 1 to 2 cm, and requires shielding on the back side to prevent generating eddy currents in the on-board electronics. The combination of shielding to constrain the field and a physical buffer limiting the minimum coil-to-coil distance will limit the cross-coupling field in most situations.

Therefore, the two requirements listed above are achieved, respectively, by using an immittance network[10] in the transmitter, and through the design of the transmitter coil geometry to achieve uniform flux density.

Transmitter Coil Design

The transmitter coil is designed to cover a 0.5-m x 0.5-m area to power all electronics from Table 1, as shown in Fig. 1b. The winding geometry is designed to achieve uniform coupling, independent of spatial positioning of the receiver.[11]

Fig. 12a shows an initial design of a 7-turn circular spiral coil with a 250-mm radius. The flux density of the coil is simulated using 2D axisymmetric FEA analysis in FEMM,[12] as shown in Fig. 13, and the resulting flux density (normalized by coil current) at a receiver surface 2 cm above the coil is shown in Fig. 12b. For the same current, a receiver placed near the inner edge of the windings will receive about double the induced voltage compared to one at the center of the coil, as shown by $|B_z|$.

An alternative coil design is shown in Fig. 14a, and its flux density in Fig. 14b. By varying the interwinding pitch between each turn, this coil has a more uniform flux density $|B_z|$ over the majority of the coil area. Therefore, this design exhibits more consistent coupling to a reference receiver coil placed at an arbitrary position over the coil. Additionally, the peak $|B|$ has been significantly reduced and now falls below the ICNIRP 2010 field exposure constraints.

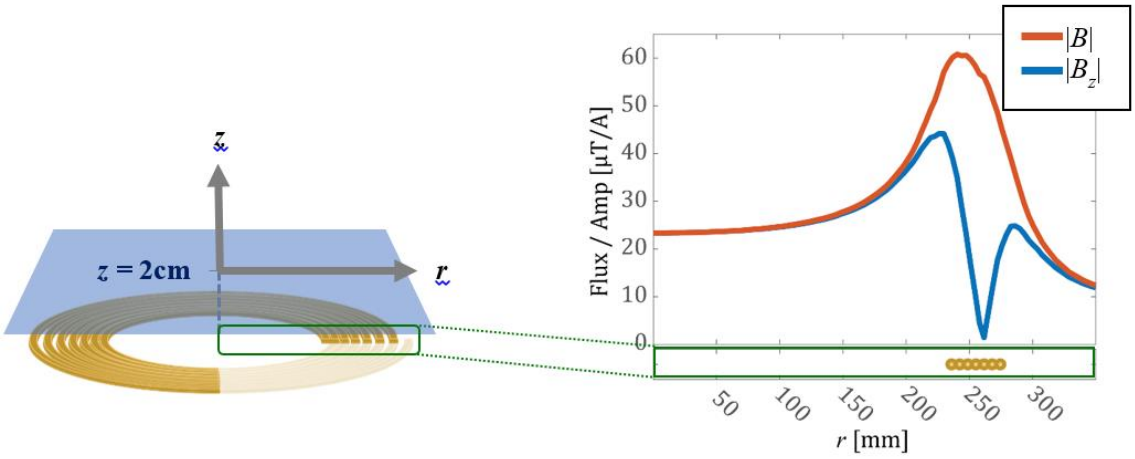

(a) (b)

Fig. 12. Example spiral coil showing axes for field measurements (a) and FEA-simulated flux density (b) on the z = 2-cm plane.

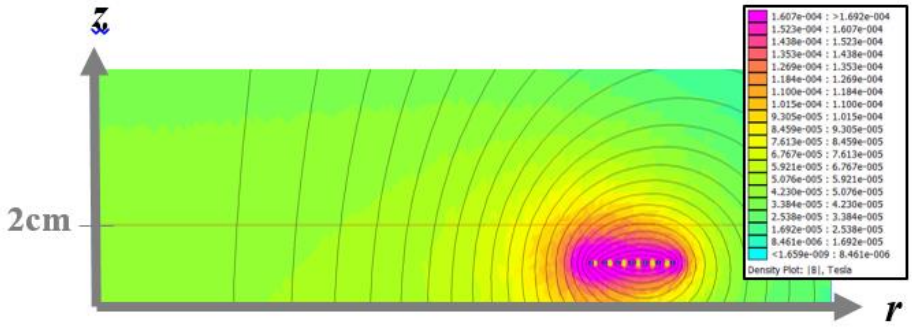

Fig. 13. FEA-simulated flux density for the coil design in Fig. 12.

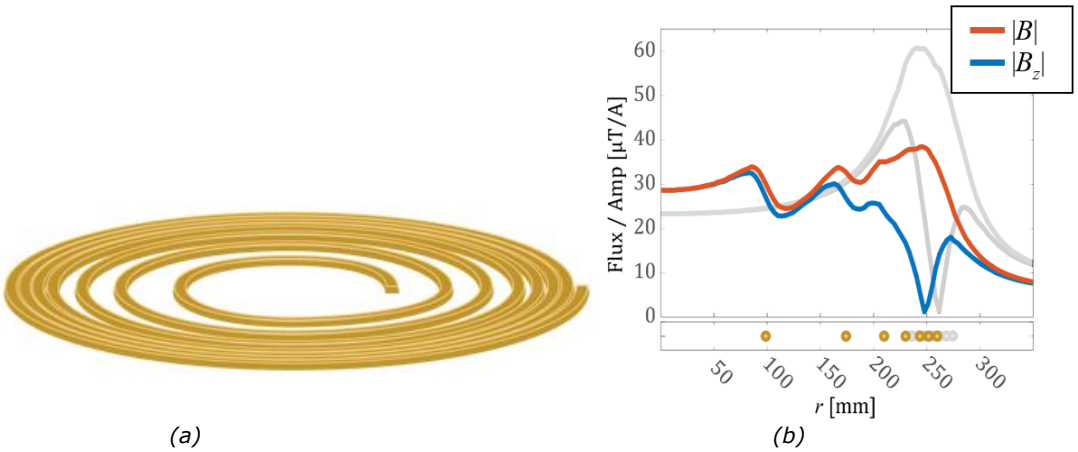

Fig. 14. A non-uniform pitch coil (a) and its resulting fields (b).

In Fig. 15, the coil is further modified to allow turns to be placed in parallel. For this example coil, the paralleling arrangement is detailed in Table 2, assuming a source current I_p driving the coil. This design achieves greater $|B_z|$ uniformity, and lower peak $|B|$; in this case the maximum $|B|$ is below the 27-μT ICNIRP 2010 exposure limit with a source current of 1 A. The average value of $|B_z|$ has decreased relative to the two previous designs, as the paralleling of turns causes the effective number of turns to reduce to just four.

To maintain current sharing near the ideal case in Table 2, each of the paralleled turns are made identical in Fig. 15a. This is done by inserting twists of paralleled turns such that each has the same total length, and uniform coupling to adjacent turns, creating balanced current in the paralleled windings. Though the current in each turn varies due to the paralleled windings, the entire coil is still driven from a single transmitter providing current I_p.

In addition to a uniform magnetic field at the receiver surface, it is desirable to have minimal electric field generation in the coil. Electric field causes safety and EMI concerns, and may generate additional losses in the dielectric medium in which the coil is mounted.

The electric filed generated due to the longitudinal voltage drop across the coil can be significantly reduced by distributing the series compensation capacitor into multiple discrete parts over the length of the coil [13,14] as shown in Fig. 16a. FEA simulations of the transmitter coil in a lossy ($\tan(\delta) = 0.02$) medium are shown in Fig. 16b, where simulations from the coil with a lumped series capacitor at the terminals, and three distributed capacitors are overlaid. The distributed compensation reduces total loss in the coil by about 1 W.

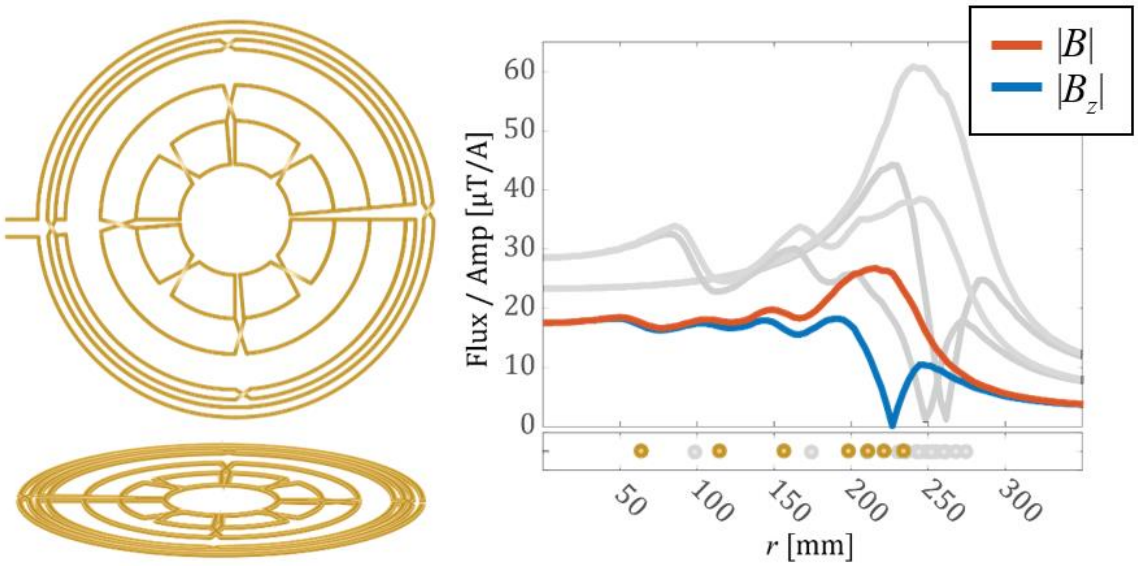

(a) (b)

Fig. 15. Coil with nonuniform pitch and parallel windings (a) and resulting fields (b).

Table 2. Paralleling arrangement for the coil of Fig. 15.

Turn	1 (outer)	2	3	4	5	6	7 (inner)
Current	I_p	I_p	$I_p/2$	$I_p/2$	$I_p/2$	$I_p/4$	$I_p/4$

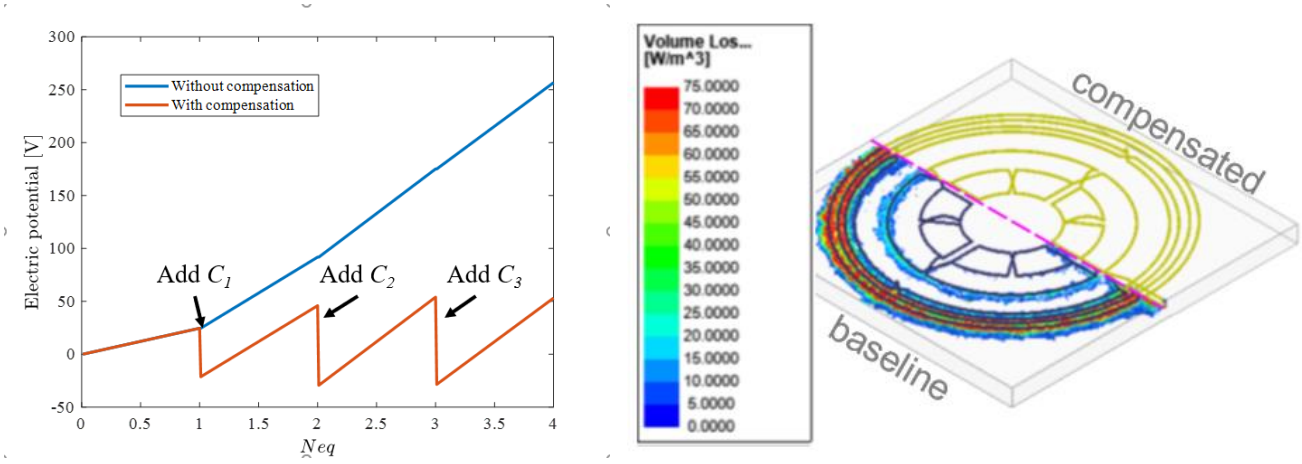

(a) (b)

Fig. 16. Longitudinal electric potential versus equivalent turn number N_{eq} with and without distributed capacitance (a) and simulated dielectric loss density for both cases (b).

A smaller prototype r = 120-mm transmitter coil is shown in Fig. 17a. The coil is fabricated with 14-AWG solid-core copper wire and designed to generate a uniform, 20-μT flux density at a height of 2 cm above the coil.

Fig. 17b shows the result of a parameter sweep of the radius and parallel winding structure of the coil, where the selected prototype is circled. The design seeks to achieve good field uniformity over the inner 80% of the coil area with minimal power loss. The resulting prototype has Q = 721 with less than 5% measured field variation within the specified area. A larger, r = 250-mm rectangular coil is designed using the same approach and used in the final system implementation.

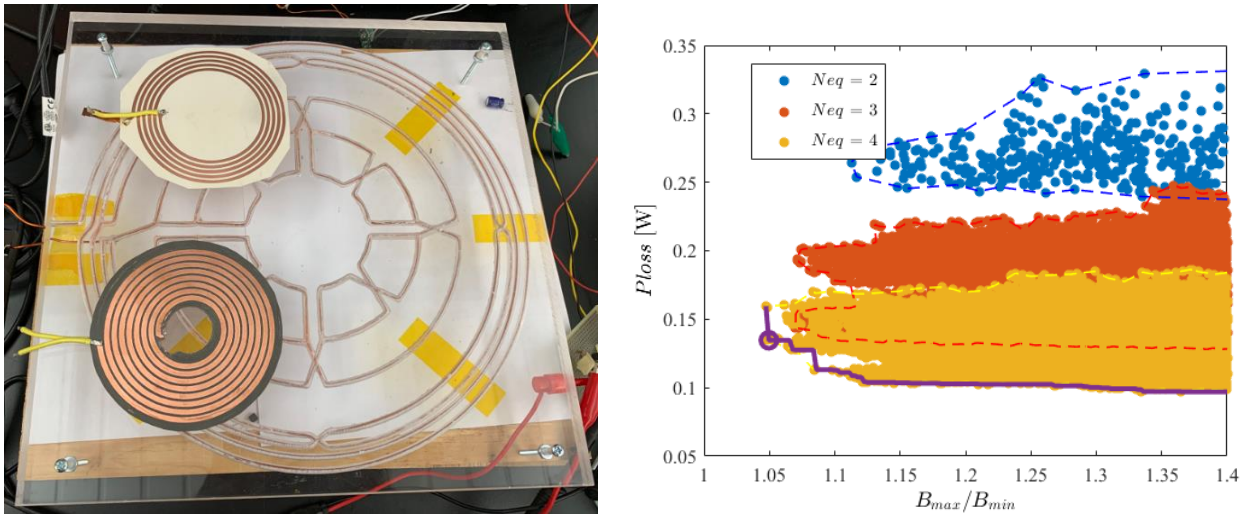

Fig. 17. A prototype transmitter coil (a) and modeled coil performance for a varying number of turns and winding geometry showing the pareto front between field uniformity and efficiency (b).

Transmitter Power Stage Design

The 6.78-MHz transmitter is implemented using a GaN-based half bridge with a ZVS tank, as shown in Fig. 18. The transmitter drives the coil (with integrated, distributed series-compensation capacitors) through an impedance matching network (IMN). In this work, the IMN consists of a T-LCL immittance network[8, 10] with $L_{mn1} = L_{mn2} = L_{mn}$ and $L_{mn} \cdot C_{mn} = (2\pi f_s)^{-2}$. The series-resonant characteristic of the coil filters all harmonics in v_{tx} except the fundamental, and the immittance network results in a coil current with a fundamental component amplitude of

$$|i_{p,1}| = \frac{v_{tx,1}}{2\pi f_s L_{mn}}$$

independent of loading impedance coupled onto the transmitter coil. Given the near-ideal voltage source behavior of the half-bridge inverter, this configuration produces a constant-amplitude coil current independent of receiver loading.

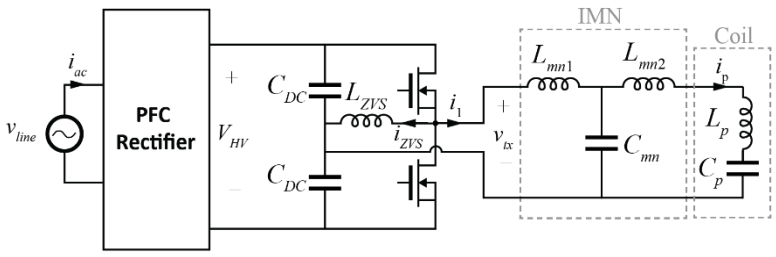

Fig. 18. Circuit schematic of 6.78-MHz transmitter.

The inverter and IMN are designed for high efficiency and power density. The inverter uses GaN Systems' GS-065-011 650-V GaN FETs and Micrometals' powder core magnetics in the IMN and ZVS tank. Using analytical loss models for the inverter operating at 6.78 MHz, with an input voltage V_{HV} = 200 V, the modeled loss of the inverter is shown for varying designs in Fig. 19.

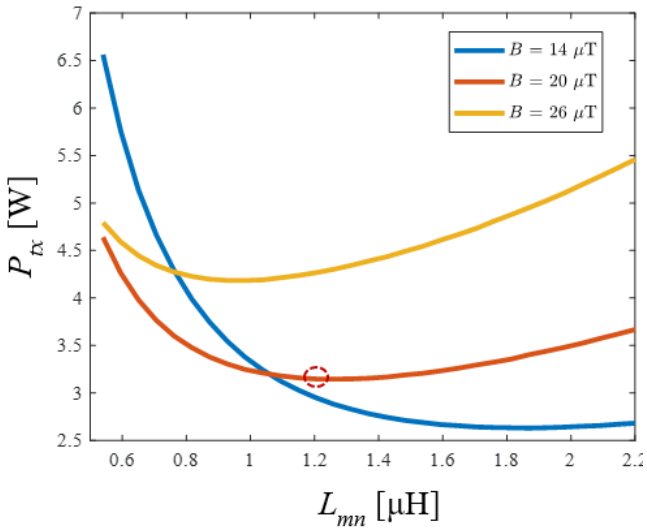

Fig. 19. Modeled loss of the transmitter for varying L_{mn} and flux density |B| at the receiver surface.

At each point, the L_{ZVS} is designed to ensure ZVS of both GaN FETs for all loading conditions. Losses in the transmitter (excluding coil loss) are shown for varying L_{mn} and flux density at the receiver surface. Although the final design point is indicated by the dashed circle, note that the model up to this point is insufficient to select an optimal system design. Selecting a flux density will impact the receiver loss. As such, the flux density is used as an intermediate variable to couple independent design sweeps of the transmitter and receiver, but the final selection requires consideration of both.

Waveforms of the 6.78-MHz transmitter are shown in Fig. 20. Accurate power measurements of the 6.78-MHz inverter output are difficult to obtain with standard lab equipment, due to the minor delays and attenuations of current probes. With two 50-W receiver coils, each loaded by a diode rectifier, the dc-dc efficiency from V_{HV} to V_{out} (Fig. 10) is 93% at 100-W output power.

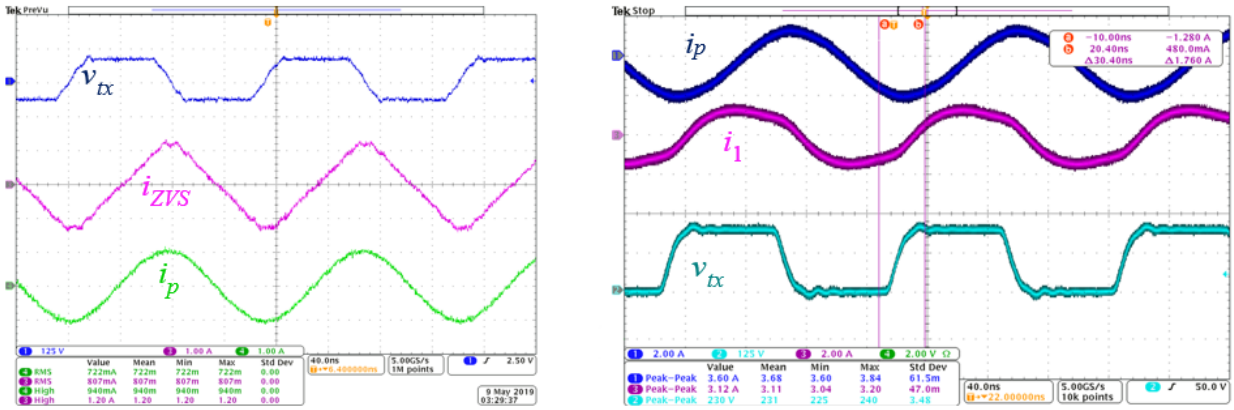

Fig. 20. Operating waveforms for the 6.78-MHz transmitter circuit at P_{out} = 0 W (a) and P_{out} = 100 W (b).

PFC Rectifier

The PFC rectifier which supplies V_{HV} is designed using a CRM totem-pole boost PFC rectifier with variable switching frequency. Design and control techniques follow those detailed in reference [15]. The PFC is implemented using 650-V GS66508B GaN FETs from GaN Systems and the same inductor core materials as the inverter. The switching frequency ranges from 300 kHz to 1.1 MHz within one line cycle of a 60-Hz, 120-Vac input.

Measured waveforms at 100-W output power are shown in Fig. 21. The rectifier has a measured efficiency of 98.3% with a power factor of 0.994 and an input current THD of 6.56%.

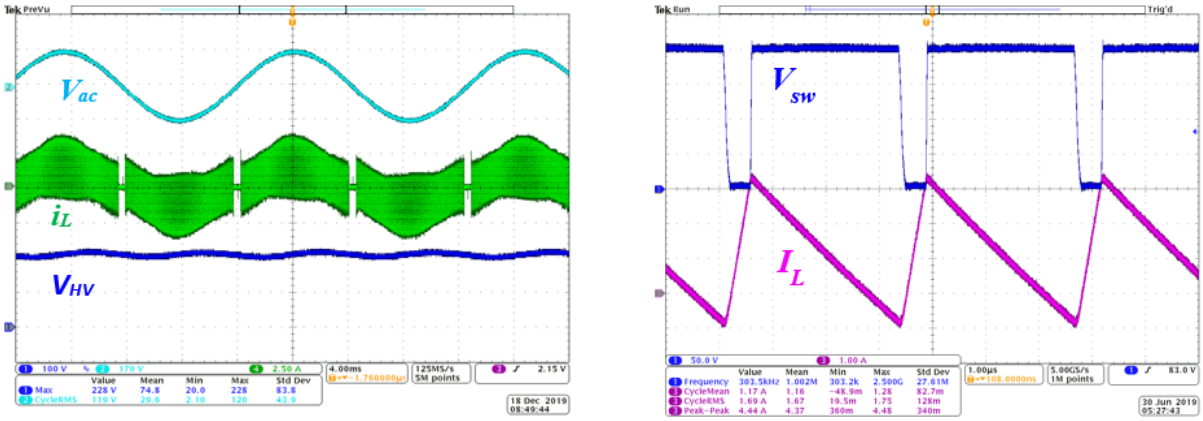

Fig. 21. Full power waveforms for the PFC rectifier over multiple 60-Hz line cycles (a) and over multiple switching periods (b).

A photo of the combined PFC rectifier and 6.78-MHz inverter hardware prototype is shown in Fig. 22. The indicated dimensions include control power, but not the controller itself; a single TMS320F2837 microcontroller provides control for both power stages. The total volume of the transmitter-side power electronics is 3.96 in^3 with a power density of 25.2 W/in^3 at the designed output power.

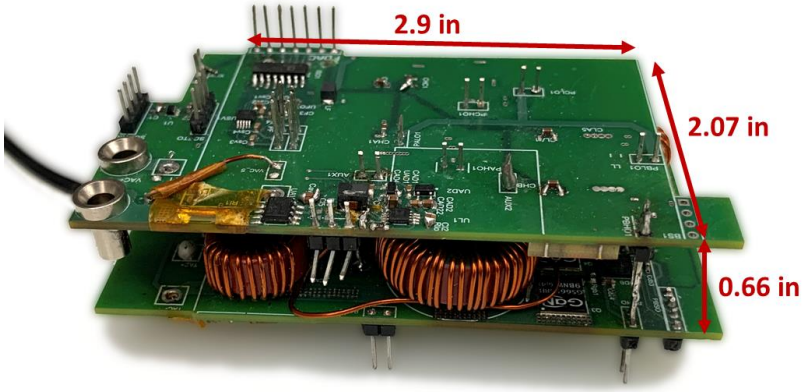

Fig. 22. Prototype of combined two-stage ac-to-RF converter.

Low-Power Receiver

A low-power receiver is designed around the LTC4120 WPT receiver IC, as shown in Fig. 23. This receiver is designed to be a seamless retrofit replacement for AA battery-powered electronics with less than 1 W of power consumption. The entire receiver, along with a Li-ion pouch cell rechargeable battery, as shown in Fig. 23a, fits within the volume of an AA battery cell.

In this design, two orthogonal receiver coils with independent diode rectifiers are used to allow sufficient coupling independent of the rotation of the module. A flexible ferrite shield surrounds the internal electronics, and a 3D-printed shell protects the coil. Contacts on either end of the module are supplied from an internal 1.5-V output dc-dc converter.

The wireless mouse in Fig. 23c has been tested and functions correctly in the WPT field generated by the transmitter. To validate power transfer, the Li-ion battery cell is removed and replaced with only a capacitor to ensure that the battery is not being powered from residual battery charge. When the mouse is placed in the transmitter coil charging area, it is able to power up and function correctly.

Fig. 23. Low-power receiver power stage (a); coil, shielding and mechanical support (b); and receiver installed in a wireless mouse.

High-Power Receiver

A separate design is used for the high-power loads. The topology, shown in Fig. 24, is based on the modeling in reference [16]. The receiver consists of a full-bridge active rectifier and a ZVS tank consisting of L_m and C_m. The ZVS tank capacitance allows the *dv/dt* of v_s to be controlled to reduce harmonic content generated by the receiver, and the inductor provides additional current to facilitate ZVS at a range of reactive loading conditions. Though not emphasized in this work, the ability to dynamically alter the reactive load presented by the rectifier, i.e Z_s, is a control freedom that can be variably used to improve system efficiency or regulate output voltage V_{out}.

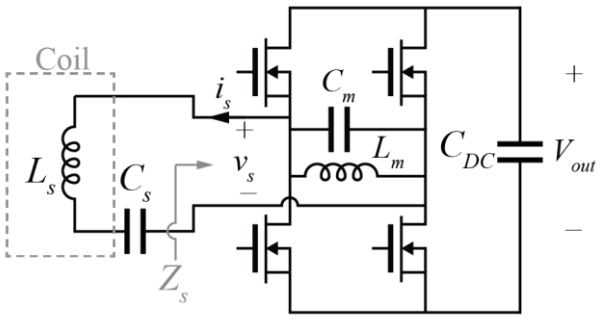

Fig. 24. High-power receiver schematic.

To employ an active rectifier as a WPT receiver, the receiver-side controller must be able to synchronize its switching frequency and phase to the transmitter without additional wired communication. The prototype high-power receiver uses techniques developed in reference [17] to synchronize the full bridge switching to the transmitter frequency, and allow a controllable phase shift between i_s and v_s.

The prototype employs an ADF4002 phase detector, an MSP430F5172 microcontroller, and an LTC6903 programmable oscillator to form a phase-locked loop between the rectifier switching actions and the sensed voltage on C_s. By injecting an offset into the output of the loop filter, the phase between these two signals is regulated by the MSP430. The power stage and control hardware for a 40-W prototype design are shown in Fig. 25.

Fig. 25. High-power receiver prototype circuit board.

The rectifier is designed using Efficient Power Conversion's EPC2007C 100-V eGaN FETs. Measured waveforms of the transmitter operation, self-synchronized to the transmitter as described previously, are shown in Fig. 26. In this experiment, the receiver output is V_{out} = 15 V and P_{out} = 27 W.

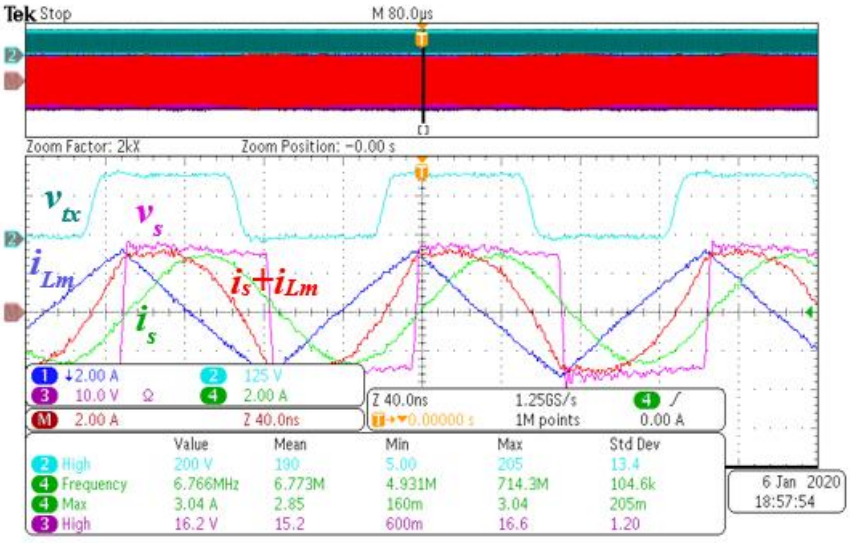

Fig. 26. Operating waveforms of the high-power receiver with self-synchronizing control.

In Fig. 26, the transmitter is switched at 6.78 MHz, with the TMS320F2837 transmitter controller deriving its clock from an external 27.12-MHz crystal oscillator. The receiver frequency is dictated by the LTC6903

oscillator, which is controlled by the MSP430. Because these two clock sources are not ideally matched, the PLL onboard the receiver continually adjusts the setpoint of the LTC6903 to maintain synchronization.

Some deviation in phase is expected due to the finite oscillator resolution and limited update rate dictated by the sampling delay of the onboard MSP430 ADC. The loop maintains locked frequency, with an average phase of −4° between v_S and i_S and an rms deviation from this average of 3°.

Experimental Testing Of Prototype System

The complete prototype WPT system, with two passive 50-W diode rectifiers, is shown in Fig. 27. For all testing, control power for the TMS320F2837 microcontroller and gate-driver-supply power are supplied separately and not included in the measurements.

A loss breakdown and comparison between modeled and measured power loss is given in Fig. 28, for operation at an output power of 100 W. Because of the difficulty in measuring the power of 6.78-MHz ac waveforms, measured efficiency is reported only for powers measured at the dc and line-frequency ac connections of the system, as shown in Fig. 29. Output power is taken as the sum of the output powers of the two receivers. The end-to-end system efficiency is 91.3%, well over the targeted goal of 90%.

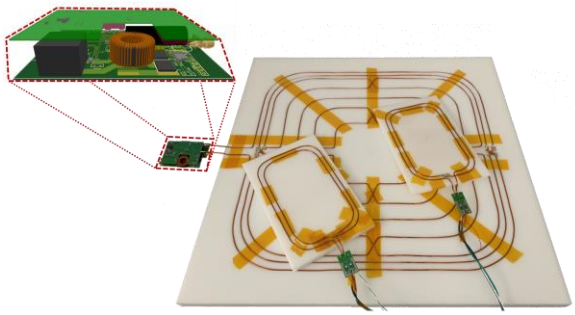

Fig. 27. Complete system with two 50-W receivers with passive diode rectifiers.

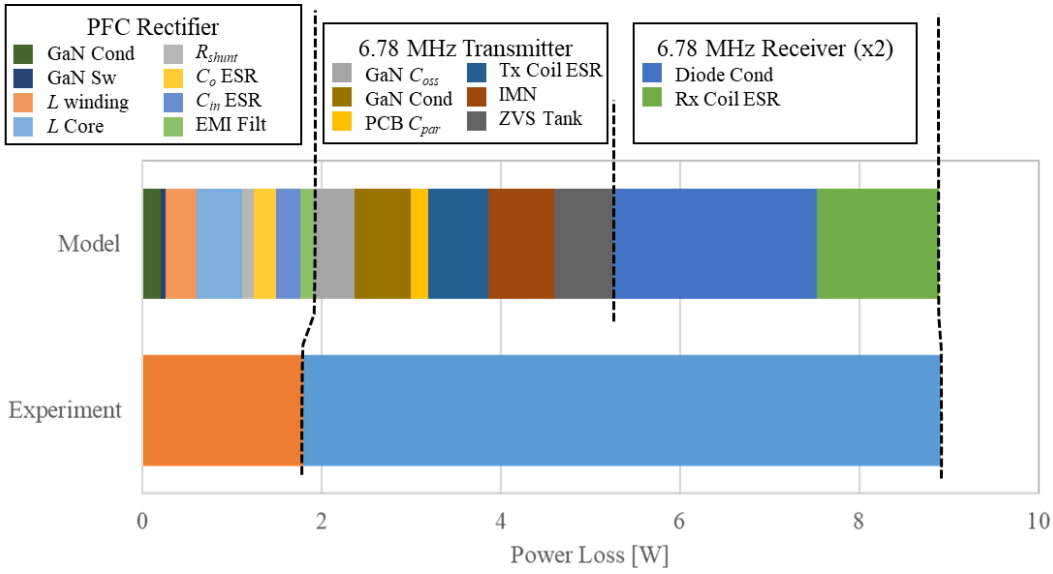

Fig. 28. Loss breakdown and comparison to experimental results for a complete system at a 100-W power level.

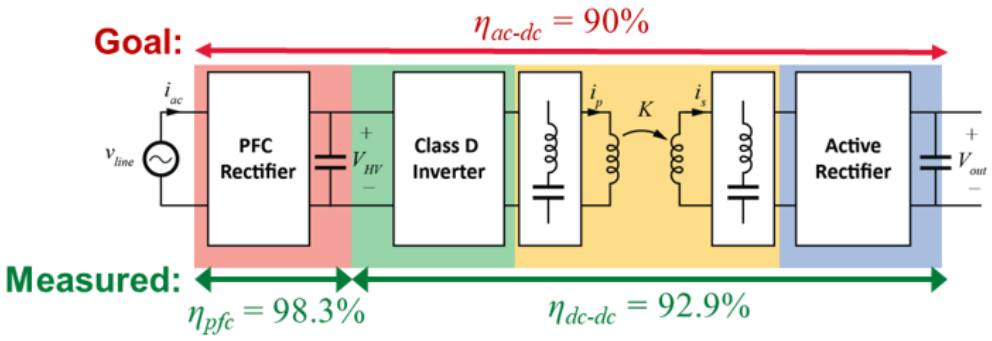

Fig. 29. Target and experimentally measured efficiencies of the prototype WPT system.

Beyond these results, ongoing work includes testing of approaches to transferring power to metal-body receivers such as laptops. Fig. 30 shows a test setup employing the active rectifier to transfer 35 W of power to a receiver with an emulated metal-body casing. Ferrite and metal shielding covering the receiver coil have been removed for this image. This configuration has been tested up to 35-W output power from the metal-body-embedded receiver.

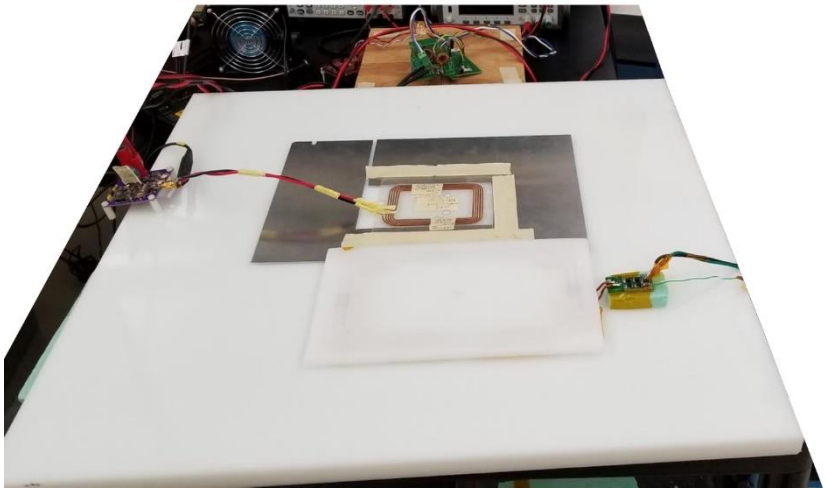

Fig. 30. Testing an active rectifier with a metal-body receiver.

Conclusion

The emergence of wide-bandgap power devices, particularly GaN transistors, has enabled new design approaches for wireless power transfer. Combined with detailed modeling and design techniques, this technology is capable of capitalizing on the promise of wireless power transfer to deliver high-efficiency, unobtrusive charging of multiple devices without constrained positioning. When incorporated into future consumer electronics, this technology could create a market for high-frequency, high-voltage, fast-switching power devices which can only be served through WBG power devices.

Future work will continue to develop comprehensive, system-level design optimization approaches, and leverage additional control freedoms in the inverter and receiver to further improve efficiency under varying operating conditions.

Acknowledgement

The information, data, or work presented herein was funded in part by the Office of Energy and Renewable Energy (EERE), U.S. Department of Energy, under Award Number DE-EE0006521-012. This work made use of the Engineering Research Center Shared Facilities supported by the Engineering Research Center Program of the National Science Foundation and DOE under NSF Award Number EEC-1041877 and the CURENT Industry Partnership Program.

References

1. "A Study of Loosely Coupled Coils for Wireless Power Transfer" by C. Chen, T. Chu, C. Lin and Z. Jou, IEEE Transactions on Circuits and Systems II: Express Briefs, vol. 57, no. 7, pp. 536-540, July 2010.

2. "Simple accurate expressions for planar spiral inductances" by S. S. Mohan, M. d. M. Hershenson, S. P. Boyd and T. H. Lee, IEEE Journal of Solid-State Circuits, vol. 34, no. 10, pp. 1419-1424, Oct. 1999.

3. "Radiation efficiency of electrically small multiturn loop antennas" by G. Smith, IEEE Transactions on Antennas and Propagation, vol. 20, no. 5, pp. 656-657, Sept. 1972.

4. "Optimal choice for number of strands in a litz-wire transformer winding" by C. R. Sullivan, IEEE Transactions on Power Electronics, vol. 14, no. 2, pp. 283-291, March 1999.

5. "ICNIRP Guidelines for Limiting Exposure to Time-Varying Electric and Magnetic Fields (1 Hz-100kHz)," International Commission on Non-Ionizing Radiation Protection Health Physics, vol. 99, no. 6, pp. 818-831, June 2010.

6. Wireless Power Consortium, a website providing information on the Qi standard.

7. The Airfuel Resonant standard. This page provides an explanation of magnetic resonance coupling.

8. "A High-Efficiency GaN-Based Single-Stage 6.78 MHz Transmitter for Wireless Power Transfer Applications" L. Jiang and D. Costinett, IEEE Transactions on Power Electronics, vol. 34, no. 8, pp. 7677-7692, Aug. 2019.

9. "A Seven-Level Switched Capacitor AC-DC Rectifier for Fast Wireless Charging" by C. Zhao, D. Costinett and S. Yang, IEEE PELS Workshop on Emerging Technologies: Wireless Power Transfer (WoW), Montréal, 2018.

10. "Immittance converters suitable for power electronics" by H. Irie and H. Yamana, Electrical Engineering in Japan, vol. 124, no. 2, p. 53–62, 1998.

11. "Optimal Design of a Hybrid Winding Structure for Planar Contactless Battery Charging Platform" by X. Liu and S. Y. Hui, IEEE Transactions on Power Electronics, vol. 23, no. 1, pp. 455-463, 2008.

12. "Finite Element Method Magnetics, Version 4.2 (28Feb2018 Build)" by D. C. Meeker.

13. "Magnetic resonance Wireless Charging for Consumer Electronic Devices Challenges and solutions" by S. Yang, IEEE Workshop on Emerging Technologies: Wireless Power (WoW), Knoxville, 2016.

14. "Distributed reactance compensation for printed spiral coils in wireless power transfer" by Y. Narusue and Y. Kawahara, IEEE Wireless Power Transfer Conference (WPTC), Taipei, 2017.

15. "Inductor Design and ZVS Control for a GaN-Based High Efficiency CRM Totem-Pole PFC Converter" by J. Sun, X. Huang, N. N. Strain, D. J. Costinett and L. M. Tolbert, IEEE Applied Power Electronics Conference and Exposition (APEC), Anaheim, 2019.

16. "Modeling a 6.78 MHz synchronous WPT rectifier with reduced THD" by S. Cochran and D. Costinett, IEEE 18th Workshop on Control and Modeling for Power Electronics (COMPEL), Stanford, 2017.

17. "Discrete Time Synchronization Modeling for Active Rectifiers in Wireless Power Transfer Systems" by S. Cochran and D. Costinett, 20th Workshop on Control and Modeling for Power Electronics (COMPEL), Toronto, 2019.

18. "A Critical Review of Recent Progress in Mid-Range Wireless Power Transfer" by S. Y. R. Hui, W. Zhong and C. K. Lee, IEEE Transactions on Power Electronics, vol. 29, no. 9, pp. 4500-4511, Sept. 2014.

About The Authors

Daniel Costinett is currently a co-director of education and diversity for the National Science Foundation/Department of Energy Research Center for Ultra-wide-area Resilient Electric Energy Transmission Networks (CURENT). He is also an associate professor in the Department of Electrical Engineering and Computer Science at the University of Tennessee, Knoxville (UTK). Additionally, Costinett is a joint faculty member in the Power Electronics and Electric Machinery Research Group, Oak Ridge National Laboratory. Prior to joining UTK, he was an instructor at Utah State University, in 2012. Costinett's research interests include resonant and soft-switching power converter design, high-efficiency wired and wireless power supplies, on-chip power conversion, medical devices and electric vehicles.

Costinett was a recipient of the National Science Foundation CAREER Award in 2017. He currently serves as associate editor of IEEE Journal of Emerging and Selected Topics in Power Electronics, and IEEE Transactions on Power Electronics. Costinett received the Ph.D. degree in electrical engineering from the University of Colorado Boulder in 2013.

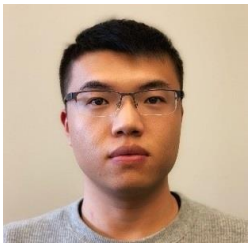

Jie Li is currently working towards a Ph.D. degree at the University of Tennessee, Knoxville, Tenn. His research interests include high-frequency power conversion, wireless power transfer and magnetics design. Li received the B.S. degree in electrical engineering from Xi'an Jiaotong University, Xi'an, China, in 2014.

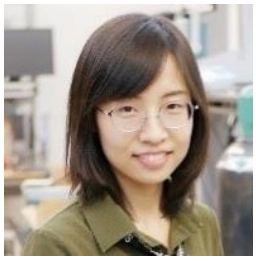

Jingjing Sun is currently a PhD student in power electronics in CURENT, University of Tennessee, Knoxville, Tenn. Her research interests are applications of wide-bandgap semiconductor devices, high-efficiency power supply design and hardware-based emulation of data center power supply systems. Sun received the B.S. degree from Xi'an Jiaotong University, Xi'an, China, in 2016, in electrical engineering, and the M.S. degree from the University of Tennessee, Knoxville in 2018.

Hoang Phuc (Peter) Pham currently is a masters candidate in electrical engineering with a specialty in power electronics at the University of Tennessee, Knoxville. His main areas of research interest are wireless power transfer, high-frequency power converters and converter control. Pham received the B.E. degree in electrical engineering from the University of Tennessee in 2018. He received the top graduate award in the same year.

For more information on designing wireless charging systems, see How2Power's Design Guide, locate the "Popular Topics" category and select "Wireless Power".